

A Realizable Version of the k - ω Turbulence Model

Uriel Goldberg

Correspondence: Uriel Goldberg , Metacomp Technologies, Inc., 28632 Roadside Drive, Suite 255, Agoura Hills, California 91301, USA.

Received: November 17, 2016 Accepted: January 6, 2017 Online Published: January 9, 2017

doi:10.11114/set.v4i1.1989

URL: <http://dx.doi.org/10.11114/set.v4i1.1989>

Abstract

This paper describes improvements in predictive quality to the original Wilcox k - ω turbulence model. A major disadvantage in the near-wall formulation of this model is usage of the *large eddy* inverse time-scale, $\omega \sim \epsilon/k$, even though small, dissipative eddies popular the immediate vicinity of walls. The present work suggests a correction to this problem through a realizable constraint introduced by the Kolmogorov time-scale. A second realizability constraint, the Schwarz condition, limits eddy viscosity magnitude in flow zones involving large normal strain gradients. Several examples demonstrate the improvements enabled due to these corrections, particularly in transonic and impinging flows where significant normal strain gradients occur.

Keywords: Turbulence model, realizable time-scale, Schwarz condition

Definitions /Abbreviations

A_k	0.0266
c	chord length [m]
C	realizability coefficient (eq. 6)
C_f	skin friction coefficient
C_p	pressure coefficient
C_μ	0.09
D	diameter [m] or diffusivity coefficient (context dependent)
D/Dt	material derivative
e	total energy [j] (eq. A2-6)
f, g, h	fluxes in x, y, z directions (eq. A1)
g_i	gravitational acceleration in i direction [m/s^2] (eq. A14)
h	channel height [m]
k	turbulence kinetic energy [$(m/s)^2$]
ℓ	length-scale [m]
M	Mach number
p	pressure [pa]
q	dependent variable vector (eq. A1)
P_k	turbulence production [m^2/s^3] (eq. 4)
R	gas constant [n m/(kg mol k)] (eq. A6)
Re	Reynolds number
Re_t	turbulence Reynolds number (eq. 6)
S	mean strain [s^{-1}] (eq. 6)
T	temperature [K]

Tu	turbulence intensity ($Tu = (\sqrt{2k/3})/U_\infty$)
u, v, w	Cartesian mean velocity components [m/s]
u', v', w'	Cartesian fluctuating velocity components [m/s]
$\overline{u'_i u'_j}$	Reynolds stress tensor [(m/s) ²]
$u_\tau = (\tau/\rho)_w^{1/2}$	friction velocity [m/s]
x, y, z	Cartesian streamwise, normal and transverse coordinates [m]
$y^+ = yu_\tau/\nu_w$	turbulent inner layer nondimensional coordinate
α	ω -eq. source term coefficient (eq. 5) or angle-of-attack [deg.] (context dependent)
β	ω -eq. sink term coefficient (eq. 5)
γ	ratio of specific heats (eq. A6)
δ	boundary layer thickness [m]
ε	turbulence kinetic energy dissipation rate [m ² /s ³]
δ_{ij}	Kronecker delta
ω	turbulence inverse time-scale [s ⁻¹]
κ	thermal conductivity coefficient [w/(m k)] (eqs. A7-9)
μ	dynamic molecular viscosity [kg/(m s)]
μ_t	dynamic eddy viscosity [kg/(m-s)]
$\nu = \mu/\rho$	kinematic molecular viscosity [m ² /s]
ρ	density [kg/m ³]
σ_k, σ_ω	turbulent diffusion coefficients (eq. 5)
σ_i	turbulence and species transport scalars (eqs. A2-9)
τ	time-scale [s] or viscous stress [pa] (context dependent)
ψ	source term vector (eq. A14)
Ω	turbulence and species source terms (eq. A14)
<i>subscripts</i>	
∞	evaluated at freestream
CL	along the center-line
i	inflow station or inviscid (context dependent)
i or j	Cartesian component in the i - or j -direction
i, j	j -direction derivative of the i -component
t or T	turbulent
v	viscous
w	evaluated at the wall
x	based on streamwise direction
0	stagnation or reference conditions (context dependent)
1	evaluated at the 1 st off-wall centroid

1. Introduction

Wilcox's popular version of the k - ω turbulence closure (Wilcox, 1988) has been a standard model choice in almost every commercial CFD solver as well as in several NASA codes and in-house flow solvers of many private companies. The Wilcox k - ω turbulence closure excels in predicting wall-bounded flows (Wilcox, 1988 and Wilcox, 1998), including those involving separation bubbles (Wilcox, 1998), but proved less than adequate in predicting hypersonic flows (Rumsey, 2009) and those involving impingement (Chima, 1996). Rumsey (2009) points out that the original k - ω model (Wilcox, 1988) performs progressively worse in wall-bounded flows – particularly for cold walls – as the Mach number increases in the hypersonic flow regime. A detailed assessment of this closure is found in Speziale, Abid & Anderson (1990) who show that “the modeled form of the ω equation that is used in the literature is incomplete - an

exact viscous term is missing which causes the model to behave in an asymptotically inconsistent manner.” Speziale et al. propose to include this viscous term and, by introducing a wall damping function with improved asymptotic behavior, their k - τ model (where $\tau = \omega^{-1}$ is the turbulent time scale) is proposed and demonstrated to be computationally robust while yielding improved predictions for turbulent boundary layers.

The present work points out that propositions like the above-mentioned k - τ closure still do not address the fundamental flaw in the near-wall formulation of the original Wilcox k - ω model (Wilcox, 1988), namely applying the large-eddy time-scale in near-wall regions where it does not belong. In order to improve predictive performance of this model, realizability constraints must be added to its formulation; one is the Schwarz condition relating Reynolds shear stresses to their corresponding normal counterparts, the other being imposition of a limit that prevents near-wall time-scales from plunging below the corresponding Kolmogorov scale. This paper shows that inclusion of these realizability constraints does improve the k - ω model’s performance in some flow situations where the original closure exhibits weaknesses.

In the next sections the new model formulation is introduced, followed by several flow examples and concluding with a summary of main findings.

2. Mathematical Formulation

Original k - ω Model Formulation

Wilcox (1988) introduced the standard k - ω turbulence closure still used by many aeronautical engineers. The model’s formulation is given by

$$\mu_t = \frac{\rho k}{\omega} \quad (1)$$

$$\frac{D(\rho k)}{Dt} = \frac{\partial}{\partial x_j} \left[\left(\mu + \frac{\mu_t}{\sigma_k} \right) \frac{\partial k}{\partial x_j} \right] + P_k - C_\mu \rho k \omega \quad (2)$$

$$\frac{D(\rho \omega)}{Dt} = \frac{\partial}{\partial x_j} \left[\left(\mu + \frac{\mu_t}{\sigma_\omega} \right) \frac{\partial \omega}{\partial x_j} \right] + \alpha \frac{\rho P_k}{\mu_t} - \beta \rho \omega^2 \quad (3)$$

Where the k -production, based on the linear Boussinesq model, is

$$P_k = \left[\mu_t \left(u_{i,j} + u_{j,i} - \frac{2}{3} u_{k,k} \delta_{ij} \right) - \frac{2}{3} \rho k \delta_{ij} \right] u_{i,j} \quad (4)$$

and the model constants are

$$\alpha=0.520, \beta=0.072, \sigma_k=\sigma_\omega=2.0, C_\mu=0.09. \quad (5)$$

There are four main limitations to the above formulation:

1. The definition of $\omega \sim \varepsilon/k$, which imposes the large eddy time-scale even in near-wall zones where it does not belong,
2. The potential overprediction of eddy viscosity in large normal-strain flow regions, due to $P_k = \nu_t S^2$ (Eq. 4),
3. The missing cross-diffusion term $\frac{2\nu}{k} \frac{\partial \omega}{\partial x_j} \frac{\partial k}{\partial x_j}$ in Eq. 3, leading to the incorrect near-wall asymptotic behavior $k \sim y^{3.23}$ instead of $k \sim y^2$ (Speziale et al., 1990 and Wilcox, 1998) as well as causing excessive sensitivity to free stream levels of ω ,
4. The linear Boussinesq model, which assumes that the principal axes of the Reynolds-stress tensor (τ_{ij}) coincide with those of the mean strain-rate tensor (S_{ij} , hence Eq. 4). This assumption is invalid in flows containing sudden changes in mean strain, flows with large curvatures, with secondary motions, rotating flows, those containing significant boundary layer separation and, in general, three-dimensional flows.

Realizable k - ω Model Formulation

The proposed formulation maintains the linear Boussinesq stress-strain assumption and concentrates on correcting the three shortcomings of the original model, indicated above as items (a) and (b), namely the incorrect near-wall time-scale and the potentially excessive eddy viscosity in high normal-strain flow regions. Two realizability constraints are introduced into the eddy viscosity formulation: One prevents the turbulence time-scale from becoming less than the

Kolmogorov scale, $\tau_t \geq \sqrt{\nu/(C_\mu k\omega)}$; the other is an isotropic equivalent of the Schwarz limiter, $\overline{u'_\alpha u'_\beta} \leq \sqrt{\overline{u'_\alpha u'_\alpha} \cdot \overline{u'_\beta u'_\beta}}$. Combined, these give rise to the following model reformulation:

$$\mu_t = \min \left\{ \frac{\rho k}{\omega} \max[1, \sqrt{2/R_t}], C \frac{\rho k}{S} \right\} \tag{6}$$

Where $R_t = v_t/\nu = k/(v\omega)$ is the turbulence Reynolds number. The first term within the braces guarantees the proper near-wall time-scale: Outside the immediate vicinity of a wall $R_t \gg 1$, hence $\max[1, \sqrt{2/R_t}] \rightarrow 1$ and the original $\mu_t = \rho k/\omega$ is recovered; within the immediate vicinity of a wall $R_t \ll 1$, hence the 1st term becomes $\sqrt{2\nu/(k\omega)} = \rho k \sqrt{2C_\mu \nu/\varepsilon}$. The Kolmogorov time-scale, $\tau_{Kol} \sim \sqrt{\nu/\varepsilon}$, is thus recovered. This and Eq. 9 also impose the near-wall behavior $v_t \sim y\sqrt{k}$. The Kolmogorov time-scale has been applied in several previously published turbulence models. Examples are Durbin (1991), Goldberg (1991), Goldberg and Apsley (1997).

The second term within the braces is an isotropic form of the Schwarz limit, using the relations $\overline{u'_i u'_i} = 3\overline{u'_1 u'_1} = 2k$ and $\overline{u'_i v'_j} = v_t S$. Applying the Schwarz constraint then yields $\mu_t \leq \frac{2\rho k}{3S}$ where the mean strain magnitude is

$$S = \sqrt{(u_{i,j} + u_{j,i} - \frac{2}{3}u_{k,k}\delta_{ij})u_{i,j}}$$

finally leading to Eq. 6 with $C=2/3$. However, as pointed out by Menter (1994), applying Bradshaw’s stress-strain relationship gives rise to $C=0.31$. The commercial solver CFD++ (Chakravarthy,

1999 and Goldberg et al., 1997), used in the current work, has both options user-selectable: $C = \begin{cases} 0.31, (\text{Bradshaw}) \\ 2/3, (\text{Schwarz}) \end{cases}$,

where the stronger Bradshaw limit is recommended for high-speed flows in order to further limit eddy viscosity magnitude due to compressibility effects. It is noted that either choice leads to a strong limit on μ_t when S is large, a situation occurring in stagnating flows and flows across normal shocks. The significance of this will become apparent in the flow examples.

While Eq. 6 imposes two kinds of realizability constraints on the final product of the turbulence closure, namely the eddy viscosity, ω itself remains singular at walls. Using fundamental viscous sublayer relationships, together with Eqs.

6 and 9, lead to $\omega \rightarrow \frac{\sqrt{A_k}}{10C_\mu} \frac{\mu}{\mu_t} S$, which becomes singular at the wall due to the vanishing of μ_t . It is also important to note

that in the viscous sublayer the 1st term within the braces in Eq. 6 is smaller than the 2nd (even if the smaller value of C ,

0.31, is used), leading to $v_t \rightarrow \frac{\sqrt{A_k}}{20} y^2 S$. The fact that v_t does not behave as y^3 is unimportant since $v_t \ll \nu$ in the immediate vicinity of walls.

The k and modified ω transport equations are:

$$\frac{D(\rho k)}{Dt} = \frac{\partial}{\partial x_j} \left[\left(\mu + \frac{\mu_t}{\sigma_k} \right) \frac{\partial k}{\partial x_j} \right] + P_k - C_{\mu} \rho k \omega \quad (7)$$

$$\frac{D(\rho \omega)}{Dt} = \frac{\partial}{\partial x_j} \left[\left(\mu + \frac{\mu_t}{\sigma_{\omega}} \right) \frac{\partial \omega}{\partial x_j} \right] + \frac{\alpha}{3} P_k \left(2 \frac{\omega}{k} + \frac{\rho}{\mu_t} \right) - \beta \rho \omega^2 \quad (8)$$

Notes: (a) The $\sqrt{2}$ factor in Eq. 6 is explained in Goldberg & Apsley, 1997, p.228. (b) The ω equation's generation term (Eq. 8) is expressed in terms of both μ_t and k/ω , unlike the original version (Eq. 3), in order to include both original (Eq. 1) and modified (Eq. 6) eddy viscosities.

In either original or modified version of the model, the boundary conditions are given as in Menter, 1994:

$$k_w = 0, \quad \omega_w = 800\nu_w/y_1^2 \quad (9)$$

Equations of Motion

All computations presented here were performed using the commercial solver CFD++ (Chakravarthy, 1999 and Goldberg et al., 1997). The numerical framework of CFD++ is based on the following general elements:

- 1) Unsteady/steady compressible and incompressible Favre-averaged Navier-Stokes equations with topography-parameter-free turbulence models.
- 2) Unification of Cartesian, structured curvilinear and unstructured grids, including hybrids.
- 3) Unified treatment of various cell shapes including hexahedral, tetrahedral and triangular prism cells (3-D), quadrilateral and triangular cells (2-D) and linear elements (1-D).
- 4) Treatment of multi-block patched aligned (nodally connected), patched-nonaligned and overset grids.
- 5) Total Variation Diminishing (TVD) discretization based on multi-dimensional interpolation framework.
- 6) Riemann solvers to provide proper signal propagation physics, including versions for preconditioned forms of the governing equations.
- 7) Consistent and accurate discretization of viscous terms using the same multi-dimensional polynomial framework.
- 8) Versatile boundary condition implementation includes a rich variety of integrated boundary condition types for the various sets of equations.
- 9) Implementation on MPP computers based on the distributed-memory message-passing model, using native message-passing libraries or MPI, PVM, etc.

The conservation form of the equations of motion is given in the Appendix.

3. Model Evaluation

The following flow examples compare the realizable and original versions of the $k-\omega$ model and illustrate the advantage of the former in some cases. All flow examples, except one, used direct solution to walls (no wall functions) achievable by (a) ensuring that y^+ at the first off-wall centroids is less than 1.0, (b) enforcing a normal-to-wall mesh growth-rate of no more than 1.20 (except for one 3D case where it is 1.25) to guarantee enough grid cells within the boundary layer, including adequate resolution of the viscous sub-layer. All reported two-dimensional grids achieved mesh-independent solutions through successive doubling of grid size. All calculations were done using double-precision computations.

The first example is that of a flat plate flow, done in order to reaffirm the expected skin friction predictions. The last two cases are three-dimensional (hypersonic and transonic) flow examples.

Practically no difference in computational efficiency was observed between the original and realizable versions of the $k-\omega$ model.

Flat Plate

A Mach 0.2 flow over a 5 m long plate serves as the first test case. The inflow is at standard atmospheric conditions with $Tu=1\%$ (where $Tu = u_{\infty}^{-1} \sqrt{\frac{2}{3} k_{\infty}}$) and $\mu_t/\mu=20$. Figure 1a shows skin friction along the plate and Figure 1b is a velocity profile at $x=4$ m. The two model versions yield almost identical results, predicting the White (1974) correlation for skin friction and the Musker (1979) velocity profile.

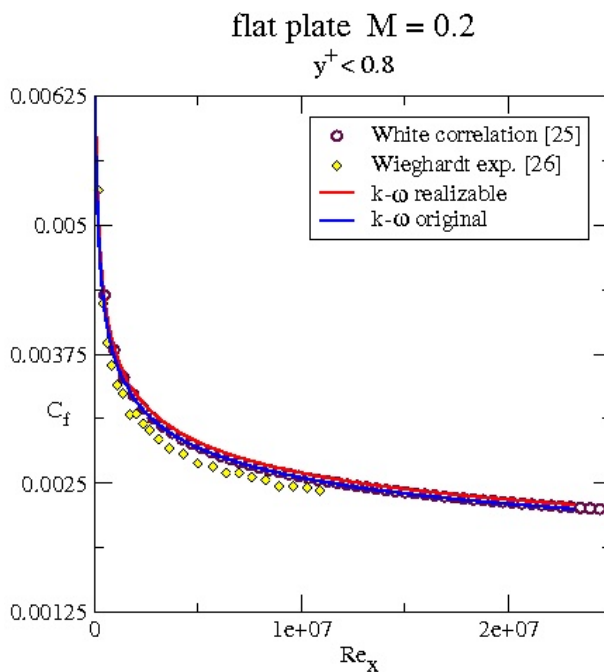


Figure 1a. C_f along plate

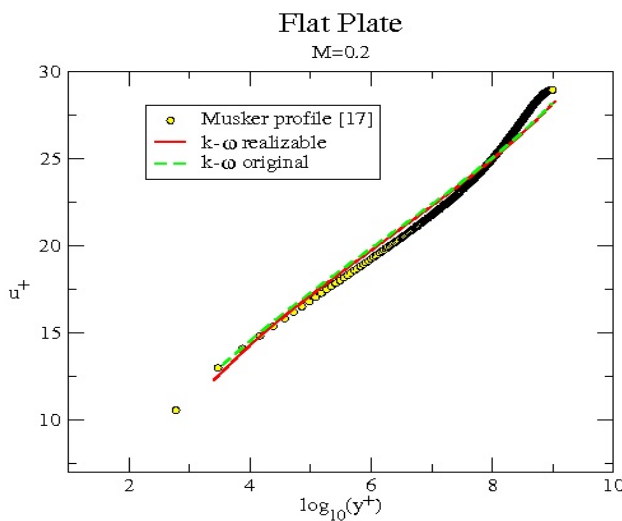


Figure 1b. Velocity profile at $x=4$ m

Backward-Facing Step

Experiments with various configurations of a backward-facing step have been reported in Driver and Seegmiller (1985). The present results are shown for the case of a parallel upper wall ($\alpha=0$ in Figure 2a). Flow details are: $M_\infty=0.128$, $T_\infty=297$ K, $p_\infty=1$ atm., $Re_h=36000$, $Tu=1\%$ and $\ell_T=2.5$ cm. Turbulent boundary layer inflow, with $\delta=1.9$ cm on both top and bottom walls, was imposed. A 92,000 cell grid with $y^+\leq 0.3$ permitted direct solution to the walls.

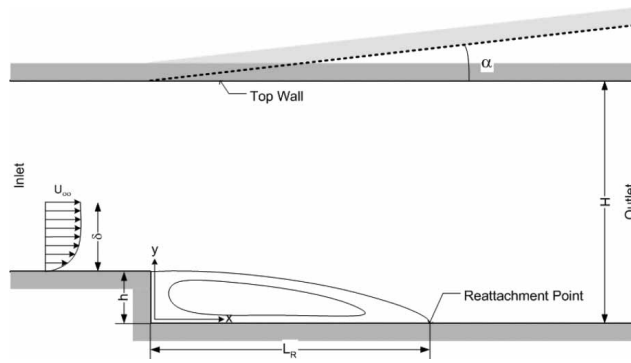


Figure 2a. Geometry and flow features

Figure 2b compares skin friction prediction, along the step-side wall, with data. The post-reattachment behavior is slightly better captured by the realizable $k-\omega$ model version. Figures 2c and 2d compare streamwise velocity and turbulence kinetic energy profiles at two locations: One inside the separation bubble, the other downstream of it. There is practically no difference between the two model versions' predictions; the velocity profiles closely follow the data whereas the k -profiles over-predict the experimental maxima (due to lack of normal stress anisotropy) but otherwise agree with the data reasonably well.

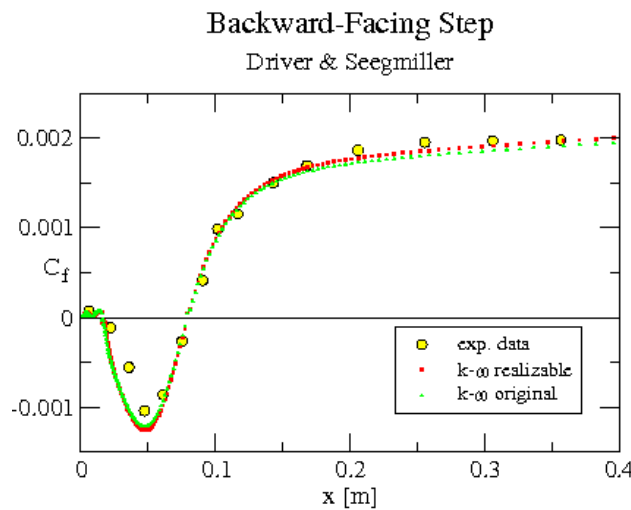


Figure 2b. Lower wall skin friction

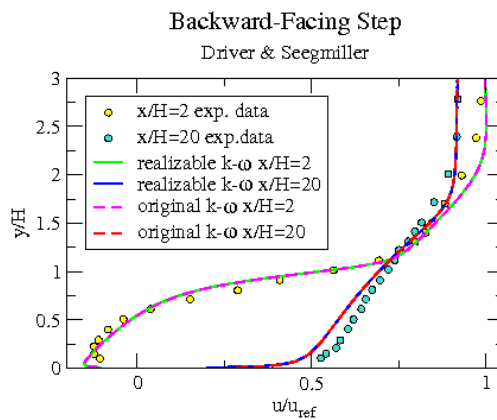


Figure 2c. Velocity profiles at two streamwise Stations; one inside the separation bubble, the other further downstream

Backward-Facing Step

Driver & Seegmiller

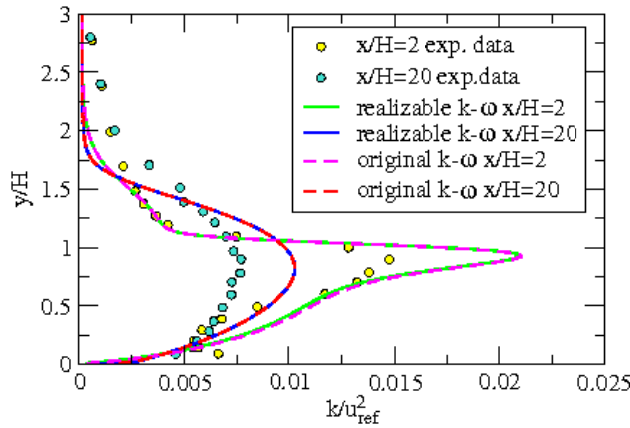


Figure 2d. k profiles corresponding to Fig. 2c

Asymmetric 2D Diffuser

Obi, Aoki & Masuda (1993) obtained experimental data for an asymmetric plane diffuser at a $Re_h=21,200$ (based on inflow centerline velocity and initial channel height, h .) Figure 3a shows the geometry and includes typical velocity contours. The diffuser is $21h$ long and the expansion angle of 10° gives an overall expansion ratio of 4.7. Corners are rounded at both ends of the diffuser with an arc radius of $4.3h$. Figure 3b provides a partial view of the mesh in the zone where flow separation is expected. Velocity and normal stress profiles at the inlet are provided (Obi et al., 1993), $U_{CL}=15.9$ m/s and the experimental data include velocity components at several streamwise locations. Neither separation nor reattachment locations are geometry-dependent, as seen in Figure 3c, therefore proper capturing of the separation bubble poses a severe challenge to turbulence models.



Figure 3a. Overall diffuser geometry and velocity contours

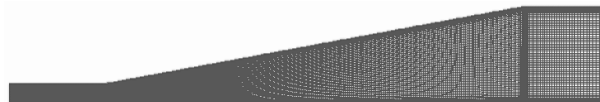


Figure 3b. Partial grid view

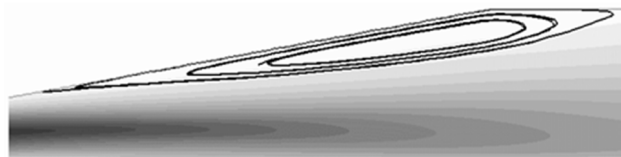


Figure 3c. Separated flow detail

The computations were done on a 45,700 cell mesh with $y^+ \approx 0.1$ on both walls and adequate grid density to capture the shear layers. Inflow kinetic energy was based on the approximation $k \approx u'^2$ for fully developed pipe flow and turbulence length-scale was chosen as $\ell_T = 1/4h$. Atmospheric conditions were used with a constant temperature of 293 K. Velocity profiles at several streamwise stations, as predicted by the two $k-\omega$ closure versions, are seen in Figures 3d. The level of agreement with data indicates satisfactory prediction of the separation bubble by both model versions.

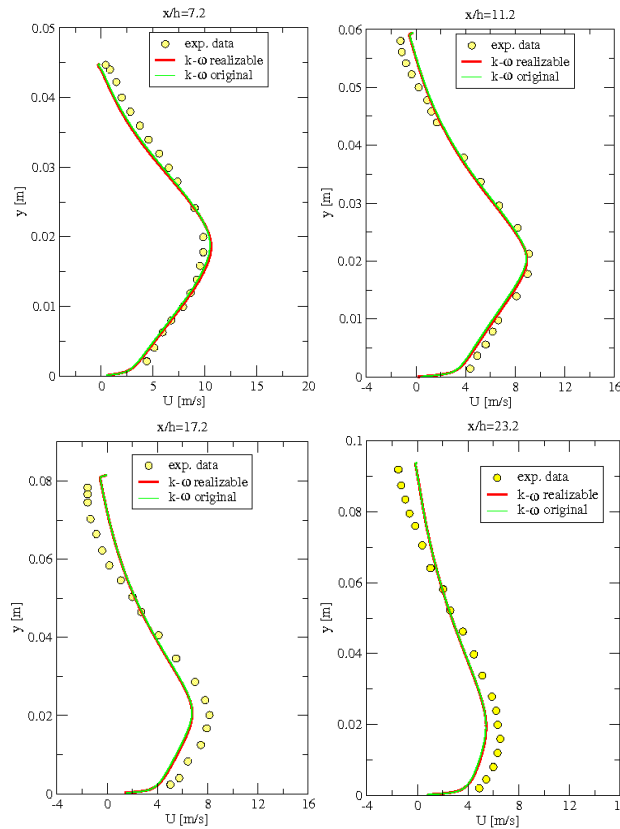


Figure 3d. Velocity profiles at several streamwise stations

Transonic Flow over an Axisymmetric Bump

This case involves transonic flow over an axisymmetric bump, reported in Bachalo and Johnson (1979). A normal shock, interacting with the boundary layer, causes flow detachment over the bump, at $x/c \approx 0.7$, with subsequent reattachment on the downstream cylindrical portion. Figure 4a shows geometry and main flow features. Inflow conditions are: $M_\infty = 0.875$, $Re_\infty = 1.36 \times 10^7/m$, $p_\infty = 57,935 \text{ Pa}$, $T_\infty = 255.6 \text{ K}$, $Tu = 1\%$ and

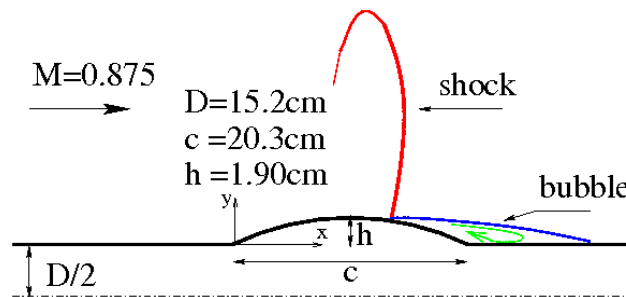


Figure 4a. Bump geometry and flow features

$\mu_t/\mu = 20$. The computations were done on a 12,000 cell grid with $y^+ \leq 1$ to permit direct solution to the wall. Both the Bradshaw and Schwarz realizability constants ($C = 0.31$ or 0.667 , Eq. 6) were invoked. Figure 4b compares wall pressure predictions with experimental data (Bachalo & Johnson, 1979), showing significantly improved performance by the realizable $k-\omega$ model with the Bradshaw constant; the Schwarz constant, however, yields a result very close to that of the original $k-\omega$ version. Figures 4c compare velocity and corresponding turbulence kinetic energy profiles at two streamwise locations; one inside the separation bubble, the other downstream of it. In spite of the much improved wall pressure predicted by the realizable $k-\omega$ version, these profiles exhibit better prediction by the original closure. This indicates that the former is superior in capturing the primary flow features, shock location and associated separation bubble, but not necessarily the near-wall flow details.

AXISYMMETRIC BUMP $M=0.875$

wall pressure

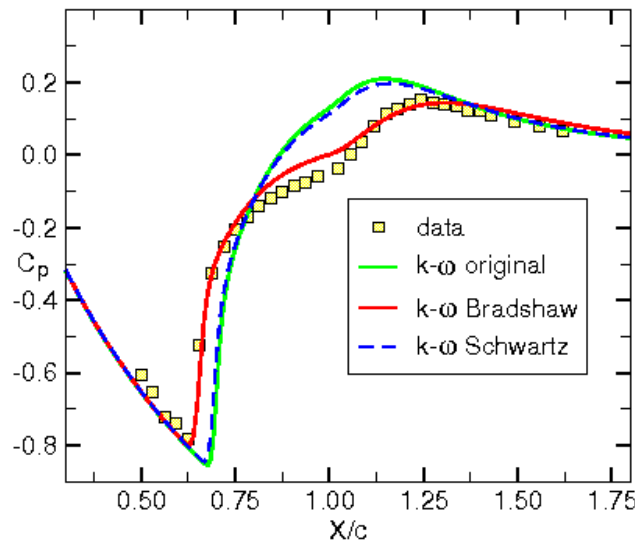


Figure 4b. Wall pressure

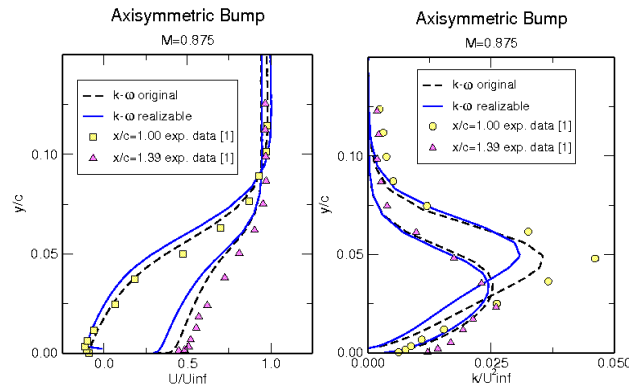


Figure 4c. (L) velocity and (R) turbulence kinetic energy profiles within and downstream of the separation bubble

Transonic Diffuser

Mohler (2005) describes a 2D transonic diffuser test case in which a subsonic inflow accelerates to supersonic levels within a nozzle-like geometry, then shocks down to subsonic flow in the diverging (diffuser) portion. The shock causes flow separation on the curved (top) wall with consequent reattachment upstream of the exit. Figure 5a illustrates the geometry and velocity contours, showing the shock and separation bubble downstream of it.

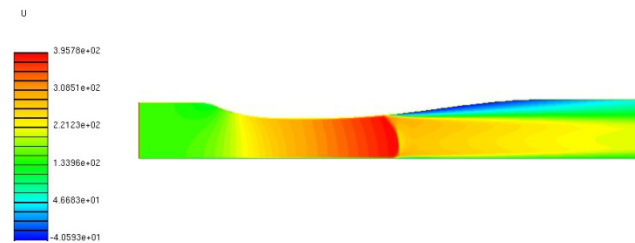


Figure 5a. Diffuser geometry and streamwise velocity contours

Flow conditions are: $p_{0,in}=134.4$ kPa, $T_{0,in}=277.8$ K, $p_{out}=97.2$ kPa, $Tu=5\%$, $\mu_t/\mu=50$.

This case was run on a 21,000 cell mesh with $y^+ \leq 0.2$ on both walls to permit direct solution to walls. Both versions of the $k-\omega$ turbulence model used compressibility correction, available in CFD++, and the new version also invoked the Bradshaw realizability constant ($C=0.31$, Eq. 6). Shock locations are considerably better predicted by the realizable $k-\omega$ version as seen in Figures 5b and 5c which compare pressure predictions along the lower and upper walls, respectively, with experimental data (Mohler, 2005). The figures include predictions by the SST model (Menter, 1994), showing almost identical results to those by the realizable $k-\omega$ closure. As in the previous case, the realizability constraints

avoid the excessive eddy viscosity predicted by the original model, thereby enabling correct prediction of shock location and resulting separation extent. This is observed in figures 5d and 5e, comparing predicted eddy viscosity by the original and realizable k- ω model versions, respectively. Higher eddy viscosity on the bottom wall and delayed separation onset (due to shock location further downstream) are clearly seen in figure 5d. Lastly, figure 5f compares predicted velocity profiles in the near-wall vicinity of the bottom surface at $x=0.33$ m, toward the diffuser exit (which is at $x=0.38$ m.) The realizable k- ω variant predicts the best agreement with the data whereas the original version underpredicts the data due to excessive turbulent diffusion. The SST model's prediction is closer to that of the realizable k- ω but deteriorates toward the wall.

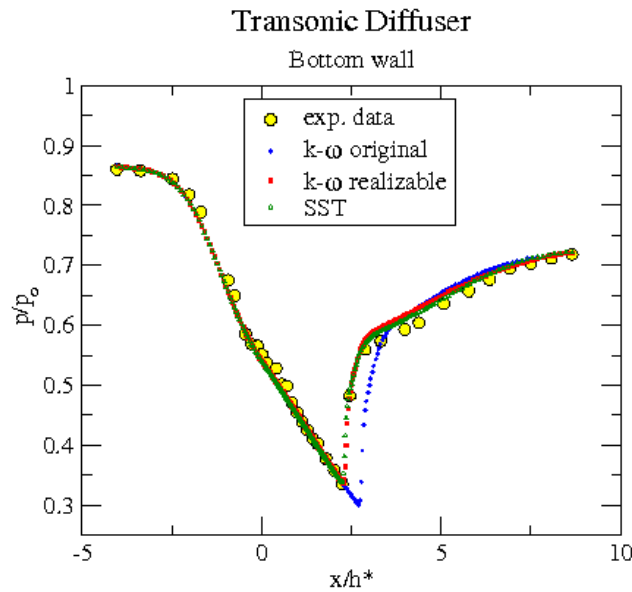


Figure 5b. Bottom wall pressure profile

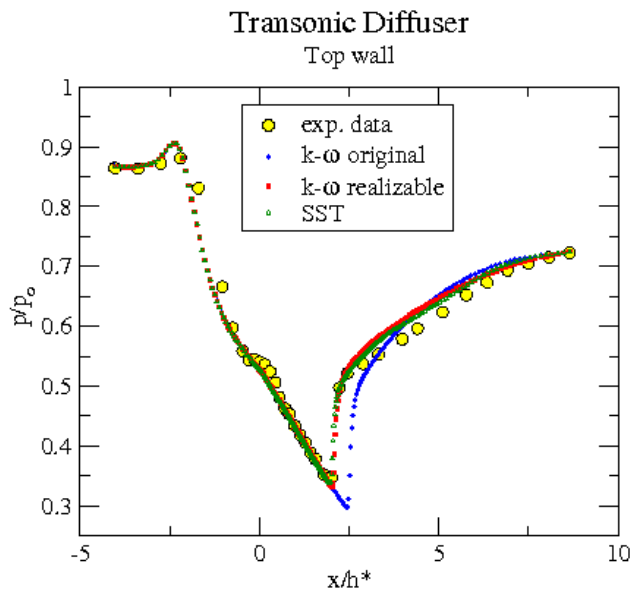


Figure 5c. Top wall pressure profile

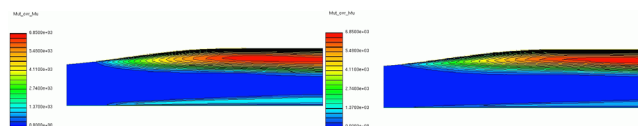


Figure 5d. Orig. k- ω μ_t/μ contours Figure 5e. Realizable k- ω μ_t/μ contours

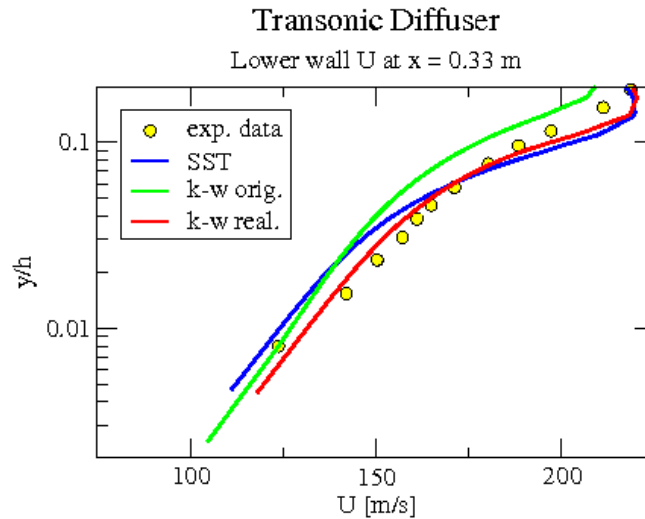


Figure 5f. Lower wall velocity profiles at x=0.33 m

Supersonic Reattaching Free Shear Layer

Samimy, Petrie & Addy (1986) report experimental results from a supersonic turbulent reattaching shear layer onto a slanted ramp (see topology, figures 6a and 6b). Freestream conditions are: $M_\infty=2.46$, $Re_\infty=5 \times 10^7/m$, $p_0=528.1$ kPa and $T_0=297$ K. An inflow boundary layer with $\delta=3.12$ mm is imposed on both walls. The $k-\omega$ turbulence models were invoked subject to $Tu=1\%$ and $\ell_1=3$ mm at inflow. A 52,500 cell grid was used for the calculation, with $y^+ \leq 0.3$ and normal-to-wall growth rate of 1.15 to enable direct solution to walls. Figure 6b shows the mesh, where the quadrilateral wall layer smoothly turns into a triangular grid inside the domain. Figure 6c shows Mach contours; the reattaching shear layer and recompression shock are clearly seen. Figure 6d shows negative streamwise velocity contours, indicating shear layer reattachment at $x \approx 139$ mm, about 7% further downstream than indicated by measurements. Figure 6e compares predicted lower wall pressure distribution with corresponding data. The original and realizable closures predict practically identical results. Figures 6f show Reynolds shear stress profiles at six streamwise locations (see figure 6a for orientation). The two model versions produce almost identical profiles which tend to overpredict the measured peak levels increasingly as moving downstream. These linear models do not have the capability to predict correctly the Reynolds stress distribution and the lack of anisotropy in the normal stresses diverts too much energy into the shear stresses, resulting in the observed overprediction of $\overline{u'v'}$. Finally, residuals in this case dropped 7 orders-of-magnitude in about 3,000 time-steps.

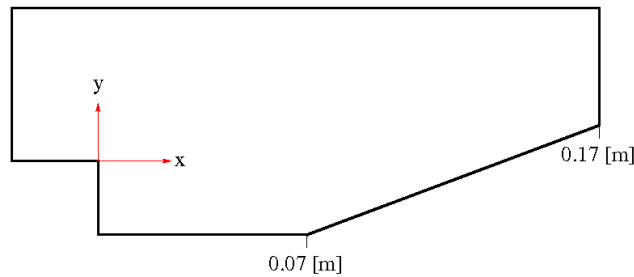


Figure 6a. Domain outline

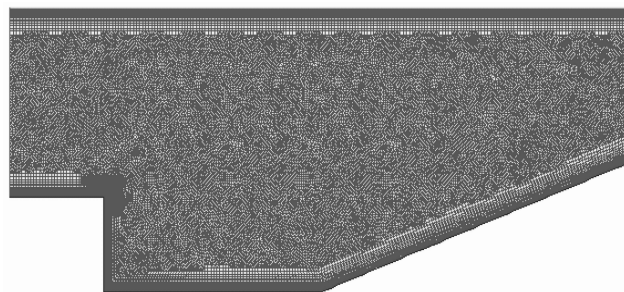


Figure 6b. Mesh topology

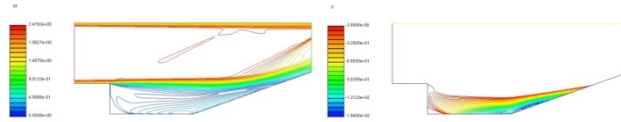


Figure 6c. Mach contours Figure 6d. Negative velocity contours

Reattaching Supersonic Shear Layer wall pressure

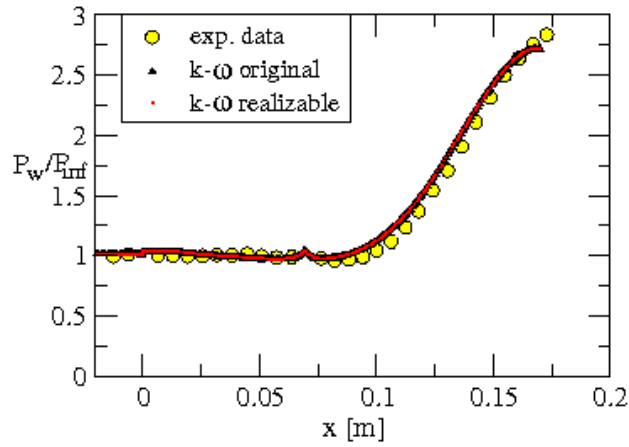


Figure 6e. Lower wall pressure profile

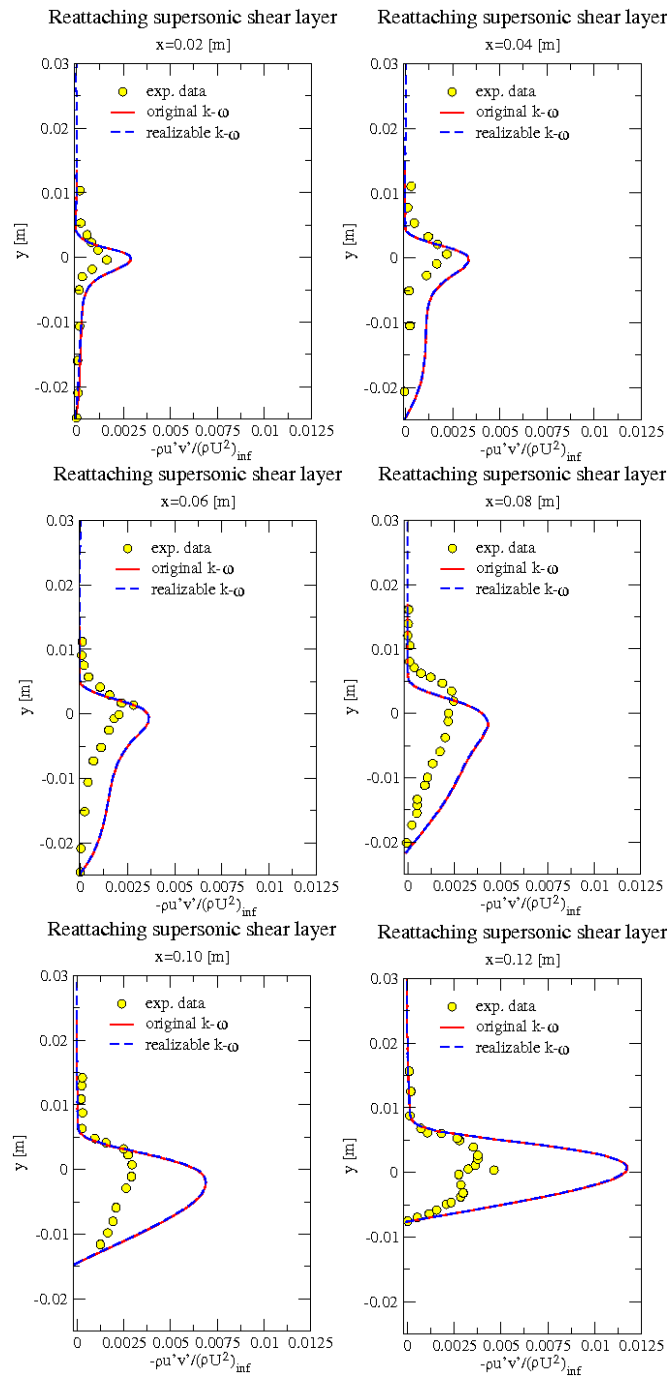


Figure 6f. Reynolds shear stress at six stations

Transonic Flow over the RAE2822 Airfoil

This case involves transonic flow over the RAE2822 airfoil, reported in Cook, McDonald & Firmin (1979), and includes a normal shock at approximately the 60% chord location. Wind-tunnel- corrected flow conditions are: $M_\infty=0.734$, $Re_c=6.5 \times 10^6$ and $\alpha=2.79^\circ$. The computation was performed on a 66,000 cell grid with $y^+ \leq 0.6$ off the airfoil and a growth ratio of 1.2. Direct solve-to-wall approach was used. The following turbulence freestream conditions were applied: $Tu=2\%$ and $l_T=1$ mm.

Figure 7a shows Mach contours with predicted shock location and Figure 7b compares C_p profiles with measured data. The shock is observed to be captured by both versions of the $k-\omega$ model in close agreement with experimental data. A slight improvement in shock location and post-shock behavior is predicted by the realizable $k-\omega$ model version.

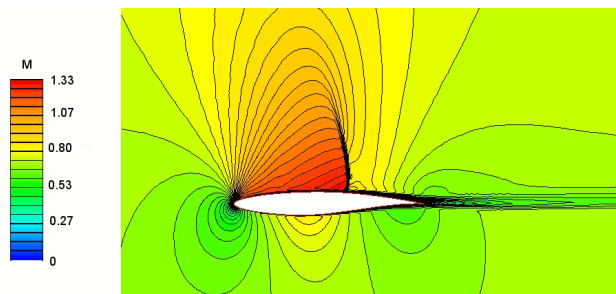


Figure 7a. Mach contours

RAE2822 airfoil

Quadrilateral mesh

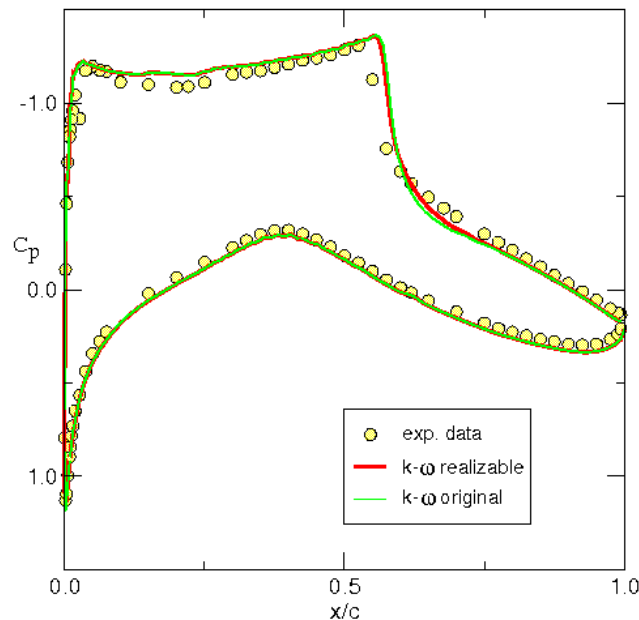


Figure 7b. Cp profiles

Impinging Flow on a Heated Wall

This axisymmetric case involves a turbulent jet from a pipe, ending 2 pipe diameters ahead of an isothermally heated plate, impinging on the plate. The shear layer from the pipe wall forms the outer boundary of this jet. As it impinges on the plate, the turbulent shear layer hits the newly developing plate boundary layer about 2 pipe diameters away from the stagnation point, where a secondary peak in heat transfer occurs due to the local increase in turbulence intensity (see figure 8a). The case for air at $Re_D = 23,000$ was computed on a 117,000 cell grid and compared with data by Baughn, Hechanova & Yan (1991) and Yan, Baughn & Mesbah (1992). Flow conditions are: $p = 10^5$ Pa, $T = 293$ K, $T_w = 314.9$ K and $D = 0.0403$ m. Figure 8a is a sketch showing topology and main flow features. To predict this flow, a 50 diameter-long adiabatic wall pipe was used to ensure a fully developed flow before the pipe end is reached. Referring to Fig. 8b, the following boundary conditions were imposed. (1) Pipe inlet: Subsonic inflow, $u = 8.715$ m/s, (2) Pipe surface: adiabatic, non-slip wall, (3) Impingement plate: Isothermal non-slip wall, (4) Far-field: p, T inflow/outflow using inside velocity (the far-field boundaries allow inflow or outflow and impose the specified ambient pressure.) Figure 8c shows an overview of the computational mesh. Calculations were performed using $Tu = 1\%$ and $\ell_T = 1.6$ cm at the pipe entrance. Near-wall mesh was fine enough ($y^+ < 1$) and sufficiently dense to integrate the equations to walls. Six orders of magnitude reduction in residuals was achieved with both model versions. Fig. 8d shows plate heat transfer predictions in Nusselt Number form. Prediction by the realizable closure is similar to that by SST and both are significantly better than the prediction by the original model in the stagnation zone.

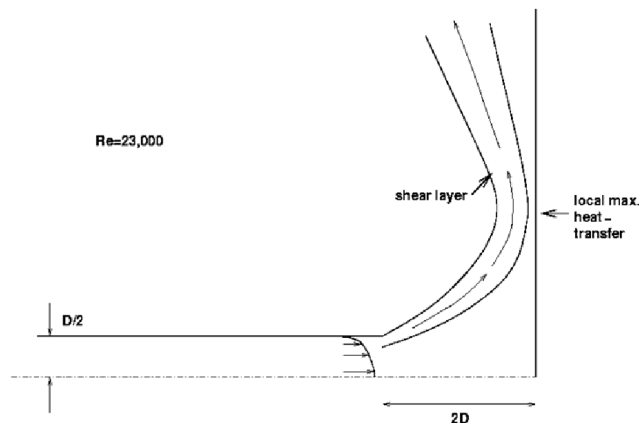


Figure 8a. Geometry and flow features

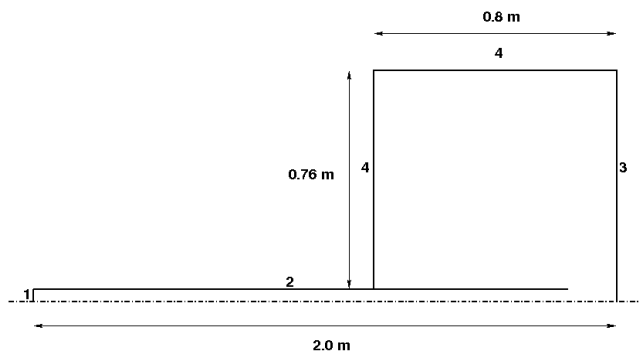


Figure 8b. Domain dimensions and boundary conditions

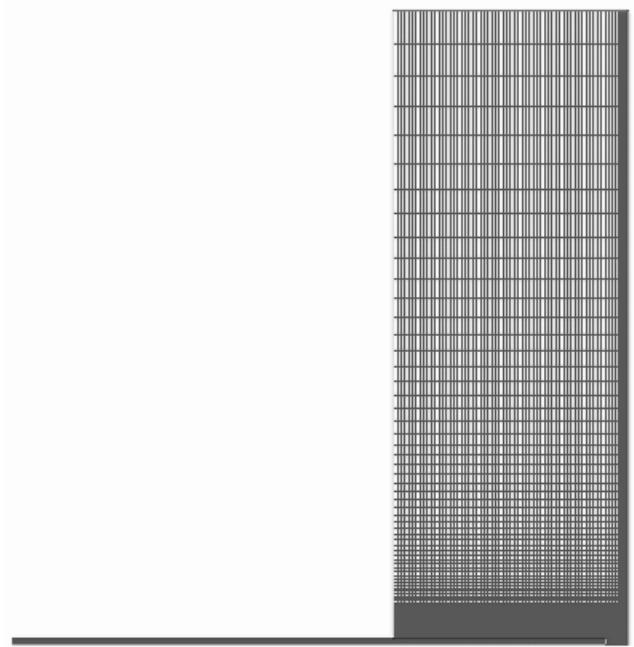


Figure 8c. Grid overview

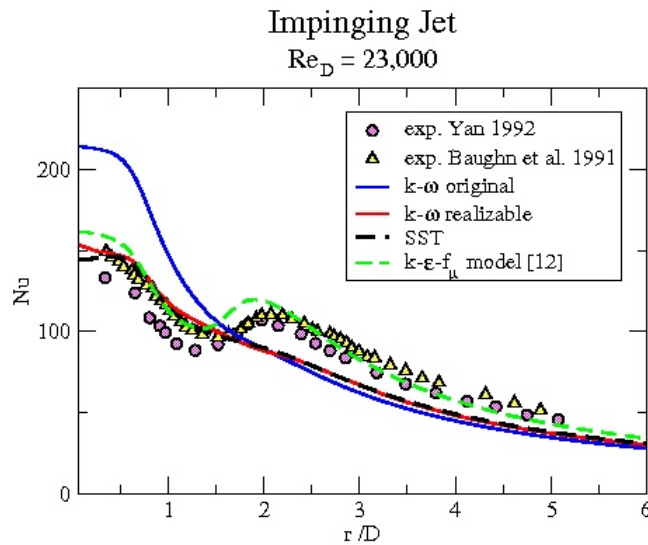


Figure 8d. Heat transfer along heated vertical plate

The secondary heat transfer peak is not predicted by either $k-\omega$ version or SST. In contrast, a solution using the $k-\epsilon-f_\mu$ turbulence closure (Goldberg and Palaniswamy, 1999), also shown in the figure, does capture the secondary peak and also improves heat transfer prediction further along the plate.

Supersonic Flow over a Compression Ramp

This test case addresses a two-dimensional $M_\infty=2.84$ flow over a 24° ramp. Measurements were reported in Dolling and Murphy (1983), Selig et al. (1989) and Settles et al. (1979). An oblique shock, impinging on the boundary layer upstream of the ramp corner (due to upstream influence), induces flow separation with subsequent reattachment onto the ramp surface. Figure 9a shows geometry and main flow features of this case and figure 9b is an overview of the computational mesh.

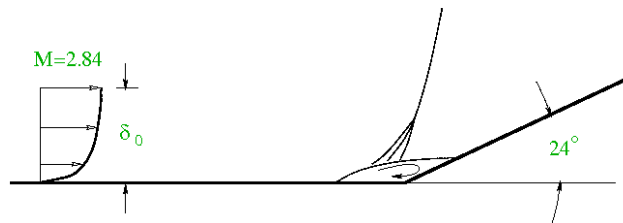


Figure 9a. Geometry and main flow features

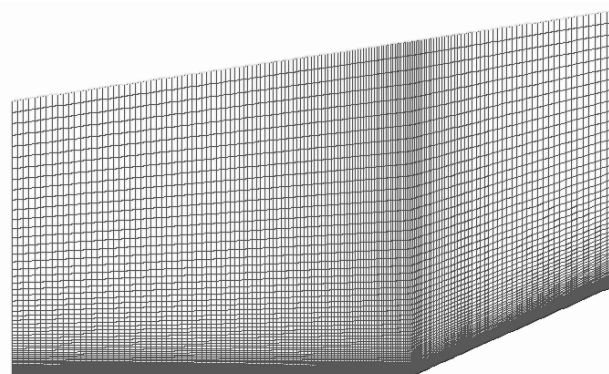


Figure 9b. Mesh overview

The solve-to-wall computations were done on a 22,200 cell grid with $y^+ \leq 0.15$. The mesh included streamwise clustering with $(\Delta x)_{min} = 0.1\delta_0$ (where $\delta_0=23$ mm), centered at the ramp’s corner. This test case is known for its sensitivity to inflow conditions (see Loyau and Vandromme, 1994). The following inflow conditions were applied: $M_\infty=2.84$, $Re_\infty=7.3 \times 10^7/m$, $T_0=262$ K, $p_\infty=24$ KPa and $T_w=276$ K, however, according to Settles et al. (1979), adiabatic conditions were imposed on the wall. The computational inflow was located $21.7\delta_0$ upstream of the corner where a

compressible equilibrium turbulent boundary layer of thickness $\delta_1/\delta_0=0.45$ was imposed. Freestream turbulence levels were set to $Tu=1\%$ and $\mu_t/\mu=10$.

Figures 9c and 9d show wall pressure and skin friction, respectively, as predicted by the two $k-\omega$ model versions. Both perform well but an advantage of the realizable closure is observed in the skin friction plot both upstream and downstream of the separation bubble. Figure 9e shows comparisons of predicted velocity profiles at the ramp corner with experimental data (Settles et al., 1979). There is little difference between the two calculations and both capture the shock location correctly.

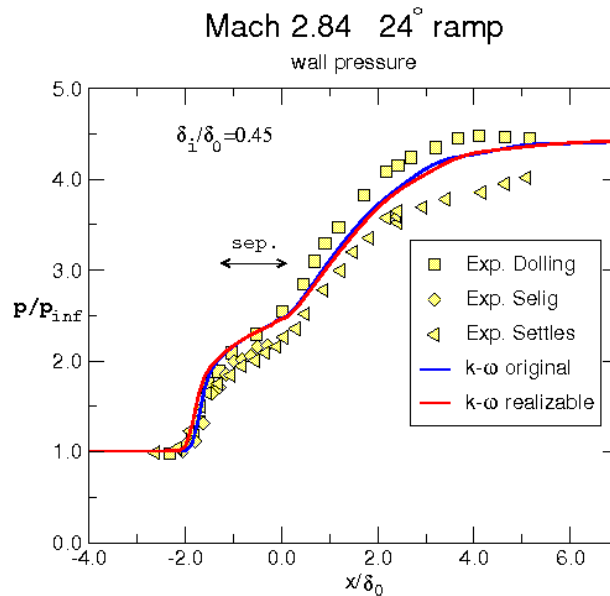


Figure 9c. Wall pressure profiles

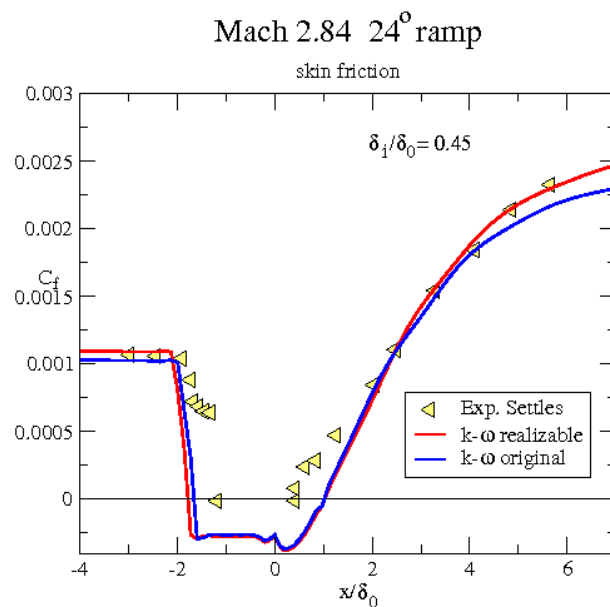


Figure 9d. Skin friction profiles

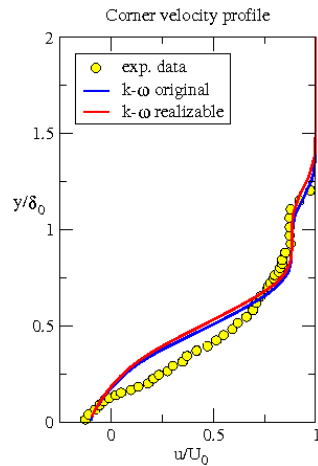


Figure 9e. Ramp corner velocity profiles

Hypersonic Flow through a Double-wedge Inlet

This test case consists of a hypersonic air flow past two sharp fins fastened to a flat test bed (figure 10a). The entire test model was kept at a constant temperature of 300 K. Kussoy, K. Horstman & C. Horstman (1993) conducted experiments using two fin geometries: One with a 10° and another with a 15° compression angle; only the latter geometry is discussed here.

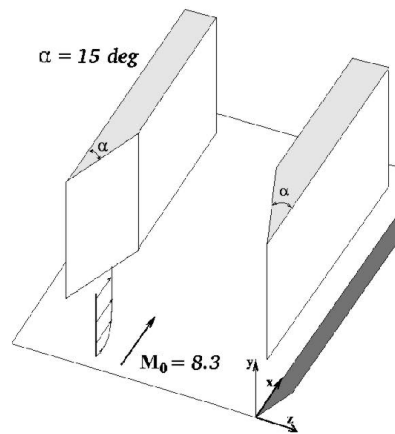


Figure 10a. Topology

The symmetry of the experimental test model was exploited in the CFD++ computations; only half the geometry was modeled, using a 972,000 cell grid comprising triangular prisms, tetrahedral, hexahedral, and pyramidal elements. Fine layers of triangular prisms were generated perpendicular to the fin and plate surfaces to properly capture the boundary layers. The first prism layer height was chosen to utilize a solve-to-wall integration approach ($y^+ < 1.0$) and the normal growth factor of the layers was 1.25. Two perpendicular planes, one at the symmetry plane, the other across the fin, show grid sections in figure 10b.

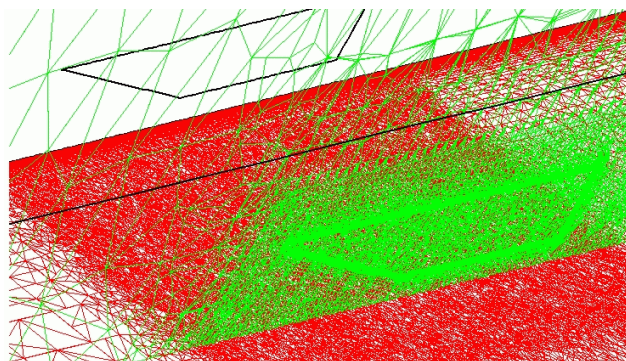


Figure 10b. Mesh around fin (green) and normal to wall (red)

The flow comes into the domain at $M_\infty=8.3$ and $T_\infty=75.2$ K. An isothermal (constant 300 K), viscous wall boundary condition is applied to the plate and fin boundaries and both are set to solve-to-wall flux integration. Since the experimental test bed was pitched at a -2° angle-of-attack to the flow, this was incorporated into the computation by a corresponding inclination of the incoming flow. Turbulence levels were set to $Tu=0.5\%$ and $\mu_t/\mu=5$. The compressible, perfect gas equation set computations reached steady-state convergence with a 5 order-of-magnitude drop in global residuals in about 1,300 time-steps. Figure 10c provides an overall view of the flowfield, showing streamline patterns around the fins. Complex recirculatory flow regions are seen downstream of the wedges while the upward direction of the streamlines downstream of the rear recirculation indicates flow displacement due both to the crossing shocks and the boundary layers. The shock/expansion pattern is observed between the wedges. Wall pressure and heat transfer along the symmetry plane are compared to experimental data in Figure 10d. Both model versions capture the pressure profile well but underpredict heat transfer levels. The realizable variant captures the peak heat transfer magnitude slightly better than the original one does and both predict the peak location correctly. It is emphasized that better predictions may be possible on a finer mesh but the aim here was to compare the two model versions on the same grid, rather than refine this 3D mesh with the hope of obtaining improved predictions.

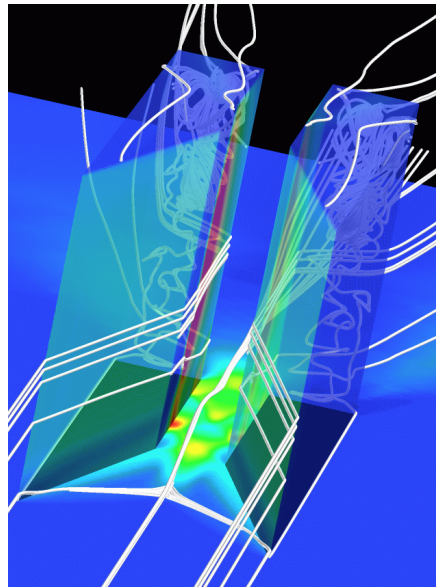


Figure 10c. Streamlines and wall pressure contours

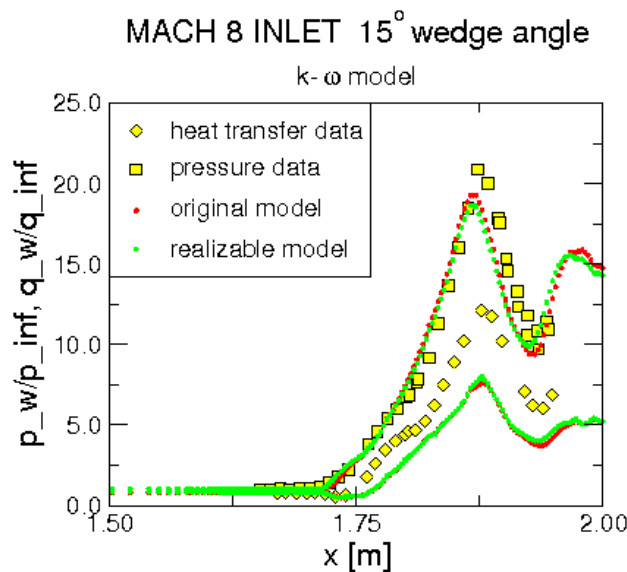


Figure 10d. Wall centerline pressure and heat transfer profiles (Kussoy et al., 1993)

Transonic Flow over the ARA M100 Wing/Fuselage Configuration

This $M=0.803$ wing/body test case, reported by Peigin and Epstein (2004), is at $\alpha=2.87^\circ$ and a chord Reynolds number

$Re_c = 13.1 \times 10^6$. The NASA mesh (cfl3d.larc.nasa.gov/Cfl3dv6/cfl3dv6_testcases.html) has 860,000 cells with an off-wall y^+ distribution as follows: $y^+_{wing}=0.8$, $0.1 \leq y^+_{fuselage} \leq 30$, the former with a growth rate of 1.1. Consequently, a wall function was used over the fuselage and direct solve-to-wall was employed on the wing. Freestream turbulence levels were $Tu=0.5\%$ and $\mu_t/\mu=25$. The realizable and original $k-\omega$ models, as well as the SST closure, were used in the calculations, the realizable $k-\omega$ being employed with both Schwarz and Bradshaw constants (C in Eq. 6). Figure 11a shows topology and pressure contours on the fuselage and upper wing surface. The normal shock footprint on the wing's suction side is observed. Figure 11b is a wing slice showing the normal shock and its interaction with the turbulent boundary layer, including flow separation. C_p profiles at two wing sections are seen in figure 11c, where $\eta=0$ and 1 correspond to wing root and tip, respectively. Comparisons with experimental data show that the original $k-\omega$ model and the realizable $k-\omega$ closure with $C=2/3$ (Schwarz constant) produce identical results, both predicting the shock location downstream of the data. The SST model, on the other hand, predicts the shock location too far upstream, indicating an overprediction of the separation region downstream of the shock. Predictions by the realizable $k-\omega$ with $C=0.31$ (Bradshaw constant) are between the former two, capturing the shock data at $\eta=0.935$ but still under-predicting it at $\eta=0.455$.

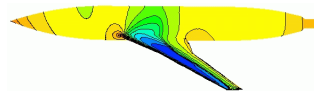


Figure 11a. Wing/fuselage

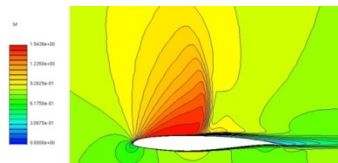


Figure 11b. Wing section showing normal shock/boundary layer interaction pressure contours

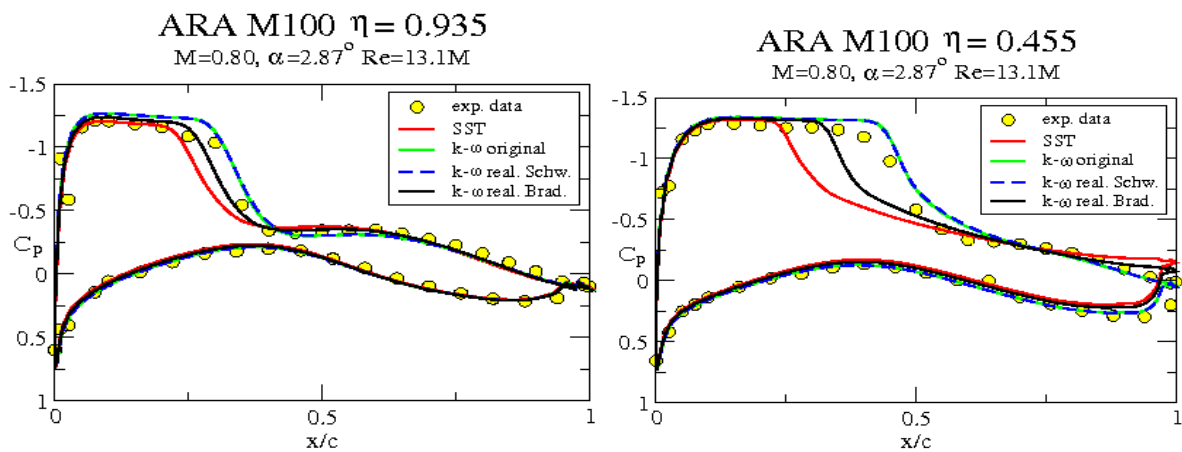


Figure 11c. C_p profiles at two wing sections

4. Summary/Conclusions

This paper focuses on implementation of realizability constraints in the original Wilcox $k-\omega$ turbulence model. These are (1) a time-scale realizability which imposes the Kolmogorov scale in the immediate vicinity of solid walls, avoiding the incorrect large eddy near-wall time-scale which exists in the original closure, (2) a Schwarz-like condition, based on k/s , that limits eddy viscosity magnitude in flow zones involving large normal strain gradients.

The other well-known impediment of the original model, namely the excessive sensitivity to freestream levels of ω , is outside the scope of the current work but has already been addressed by Menter (1994) and led to the SST closure.

Comparing the performances of the original and realizable versions of the $k-\omega$ turbulence model, in both two- and three-dimensional flow cases, leads to the conclusion that the latter yields superior predictions mainly for transonic flows and those involving impingement, where large normal strain gradients occur, while behaving similar to or marginally better than the original closure in other flow regimes. Thus the proposed realizable version seems worth recommending to researchers who routinely use the $k-\omega$ turbulence closure.

Future effort will focus on more three-dimensional flow cases at various Mach number regimes in order to better establish the scope of the realizable model's advantages.

References

- Bachalo, W. D., & Johnson, D. A. (1979). An Investigation of Transonic Turbulent Boundary Layer Separation Generated on an Axisymmetric Flow Model, *AIAA Paper*, 79-1479. <https://doi.org/10.2514/6.1979-1479>
- Baughn, J. W., Hechanova, A., & Yan, X. (1991). An Experimental Study of Entrainment Effects on the Heat Transfer From a Flat Plate Surface to a Heated Circular Impinging Jet, *ASME J. Heat Transfer*, 113, 1023-1025. <https://doi.org/10.1115/1.2911197>
- Chakravarthy, S. (1999). A Unified-Grid Finite Volume Formulation for Computational Fluid Dynamics, *Int. J. Numer. Meth. Fluids*, 31, 309-323. [https://doi.org/10.1002/\(SICI\)1097-0363\(19990915\)31:1<309::AID-FLD971>3.0.CO;2-M](https://doi.org/10.1002/(SICI)1097-0363(19990915)31:1<309::AID-FLD971>3.0.CO;2-M)
- Chima, R. V. (1996). A $k-\omega$ Turbulence Model for Quasi-Three-Dimensional Turbomachinery Flows, *AIAA paper*, 96-0248. <https://doi.org/10.2514/6.1996-248>
- Cook, P. H., McDonald, M. A., & Firmin, M. C. P. (1979). Aerofoil RAE 2822 - Pressure Distributions and Boundary Layer and Wake Measurements, Experimental Data Base for Computer Program Assessment, *AGARD Report AR*, 138.
- Dolling, D. S., & Murphy, M. T. (1983). Unsteadiness of the Separation Shock Wave Structure in a Supersonic Compression Ramp Flowfield, *AIAA Journal*, 21, 1628-1634. <https://doi.org/10.2514/3.60163>
- Driver, D. M., & Seegmiller, H. L. (1985). Features of a Reattaching Turbulent Shear Layer in Divergent Channel Flow, *AIAA Journal*, 23, 163-171. <https://doi.org/10.2514/3.8890>
- Durbin, P. A. (1991). Near-Wall Turbulence Closure Modeling Without ‘Damping Functions’, *Theoretical and Computational Fluid Dynamics*, 3, 1-13.
- Goldberg, U. C. (1991). Derivation and Testing of a One-Equation Model Based on Two Time Scales, *AIAA Journal*, 29, 1337-1340. <https://doi.org/10.2514/3.10741>
- Goldberg, U., & Apsley, D. (1997). A Wall-Distance-Free Low Re $k-\epsilon$ Turbulence Model, *Computer methods in applied mechanics and engineering*, 145, 227-238. [https://doi.org/10.1016/S0045-7825\(96\)01202-9](https://doi.org/10.1016/S0045-7825(96)01202-9)
- Goldberg, U., & Palaniswamy, S. (1999). The $k-\epsilon-f_{\mu}$ Turbulence Closure Model, *Comput. Methods Appl. Mech. Engrg.*, 179, 139-149. [https://doi.org/10.1016/S0045-7825\(99\)00035-3](https://doi.org/10.1016/S0045-7825(99)00035-3)
- Goldberg, U., Peroomian, O., Chakravarthy, S., & Sekar, B. (1997). Validation of CFD++ Code Capability for Supersonic Combuster Flowfields, *AIAA Paper*, 97-3271.
- Kussoy, M. I., Horstman, K. C., & Horstman, C. C. (1993). Hypersonic Crossing Shock-Wave/Turbulent-Boundary-Layer Interactions, *AIAA Journal*, 31, 2197-2203. <https://doi.org/10.2514/3.11915>
- Loyau, H., & Vandromme, D. (1994). TC5 Workshop Synthesis, *Proc. ETMA workshop*, UMIST, Manchester, U.K.
- Menter, F. R. (1994). Two-Equation Eddy-Viscosity Turbulence Models for Engineering Applications, *AIAA Journal*, 32, 1598-1605. <https://doi.org/10.2514/3.12149>
- Mohler, S. R. (2005). Wind-US Unstructured Flow Solutions for a Transonic Diffuser, *NASA CR-2005-213417*.
- Musker, A. J. (1979). Explicit Expression for the Smooth Wall Velocity Distribution in a Turbulent Boundary Layer, *AIAA Journal*, 17, 655-657. <https://doi.org/10.2514/3.61193>
- Obi, S., Aoki, K., & Masuda, S. (1993). Experimental and Computational Study of Turbulent Separating Flow in an Asymmetric Plane Diffuser, *9th Symposium on Turbulent Shear Flows*, Kyoto, Japan.
- Peigin, S., & Epstein, B. (2004). Embedded Parallelization Approach for Optimization in Aerodynamic Design, *Journal of Supercomputing*, 29(3), 243-263. <https://doi.org/10.1023/B:SUPE.0000032780.68664.1b>
- Rumsey, C. L. (2009). Compressibility Considerations for $k-\omega$ Turbulence Models in Hypersonic Boundary Layer Applications, *NASA/TM-2009-215705*.
- Samimy, M., Petrie, H. L., & Addy, A. L. (1986). A Study of Compressible Turbulent Reattaching Free Shear Layers, *AIAA Journal*, 24, 261-267. <https://doi.org/10.2514/3.9254>
- Selig, M. S., Andreopoulos, J., Muck, K. C., Dussauge, J. P., & Smits, A. J. (1989). Turbulence Structure in a Shock Wave/Boundary Layer Interaction, *AIAA Journal*, 27, 862-869. <https://doi.org/10.2514/3.10193>

- Settles, G. S., Fitzpatrick, T. J., & Bogdonoff, S. M. (1979). Detailed Study of Attached and Separated Compression Corner Flowfields in High Reynolds Number Supersonic Flow, *AIAA Journal*, 17, 579-585. <https://doi.org/10.2514/3.61180>
- Speziale, C. G., Abid, R., & Anderson, E. C. (1990). A Critical Evaluation of Two-Equation Models for Near Wall Turbulence, *NASA CR 182068* and *ICASE Report* No. 90-46.
- White, F. M. (1974). *Viscous fluid flow*, 1st ed., McGraw-Hill Inc. 498-499.
- Wilcox, D. C. (1988). Reassessment of the Scale-Determining Equation for Advanced Turbulence Models, *AIAA Journal* 26, 1299-1310. <https://doi.org/10.2514/3.10041>
- Wilcox, D. C. (1998). *Turbulence modeling for CFD*, 2nd Ed., ISBN 0-9636051-5-1.
- Yan, X., Baughn, J. W., & Mesbah, M. (1992). The Effect of Reynolds Number on the Heat Transfer Distribution from a Flat Plate to an Impinging Jet, *ASME Heat Transfer Division*, 226, 1-7. cfl3d.larc.nasa.gov/Cfl3dv6/cfl3dv6_testcases.html

Appendix

Conservation Form of the Equations of Motion

$$\frac{\partial q}{\partial t} + \frac{\partial(f_i - f_v)}{\partial x} + \frac{\partial(g_i - g_v)}{\partial y} + \frac{\partial(h_i - h_v)}{\partial z} = \Psi \quad (\text{A1})$$

$$q = (e \rho \rho u \rho v \rho w \rho \sigma_1 \cdots \rho \sigma_N)^T \quad (\text{A2})$$

$$f_i = ((e + p)u \rho u \rho u^2 + p \rho uv \rho uw \rho u \sigma_1 \cdots \rho u \sigma_N)^T \quad (\text{A3})$$

$$g_i = ((e + p)v \rho v \rho v u \rho v^2 + p \rho vw \rho v \sigma_1 \cdots \rho v \sigma_N)^T \quad (\text{A4})$$

$$h_i = ((e + p)w \rho w \rho w u \rho w v \rho w^2 + p \rho w \sigma_1 \cdots \rho w \sigma_N)^T \quad (\text{A5})$$

$$p = \rho R T = (\gamma - 1) \left(e - \frac{\rho}{2} u_i u_i \right) \quad (\text{A6})$$

$$f_v = \left(\kappa \frac{\partial T}{\partial x} + u \tau_{xx} + v \tau_{xy} + w \tau_{xz} \quad 0 \quad \tau_{xx} \quad \tau_{xy} \quad \tau_{xz} \quad \rho D \frac{\partial \sigma_1}{\partial x} \cdots \rho D \frac{\partial \sigma_N}{\partial x} \right)^T \quad (\text{A7})$$

$$g_v = \left(\kappa \frac{\partial T}{\partial y} + u \tau_{yx} + v \tau_{yy} + w \tau_{yz} \quad 0 \quad \tau_{yx} \quad \tau_{yy} \quad \tau_{yz} \quad \rho D \frac{\partial \sigma_1}{\partial y} \cdots \rho D \frac{\partial \sigma_N}{\partial y} \right)^T \quad (\text{A8})$$

$$h_v = \left(\kappa \frac{\partial T}{\partial z} + u \tau_{zx} + v \tau_{zy} + w \tau_{zz} \quad 0 \quad \tau_{zx} \quad \tau_{zy} \quad \tau_{zz} \quad \rho D \frac{\partial \sigma_1}{\partial z} \cdots \rho D \frac{\partial \sigma_N}{\partial z} \right)^T \quad (\text{A9})$$

$$\tau_{xx} = 2(\mu + \mu_t) \left(\frac{\partial u}{\partial x} - \frac{1}{3} \bar{v} \cdot \bar{v} \right) \quad (\text{A10})$$

$$\tau_{yy} = 2(\mu + \mu_t) \left(\frac{\partial v}{\partial y} - \frac{1}{3} \bar{v} \cdot \bar{v} \right) \quad (\text{A11})$$

$$\tau_{zz} = 2(\mu + \mu_t) \left(\frac{\partial w}{\partial z} - \frac{1}{3} \bar{v} \cdot \bar{v} \right) \quad (\text{A12})$$

$$\tau_{ij} = (\mu + \mu_t) \left(\frac{\partial u_i}{\partial x_j} + \frac{\partial u_j}{\partial x_i} \right) \quad (\text{A13})$$

$$\Psi = (0 \quad 0 \quad g_x \quad g_y \quad g_z \quad \Omega_1 \cdots \Omega_N)^T \quad (\text{A14})$$

Copyrights

Copyright for this article is retained by the author(s), with first publication rights granted to the journal.

This is an open-access article distributed under the terms and conditions of the [Creative Commons Attribution license](#) which permits unrestricted use, distribution, and reproduction in any medium, provided the original work is properly cited.